Supplementary Information of Localized Dissipation in Linear Moiré Heat Transport

1. Thermal conductivity in one four-site unit-cell

The conductivity distribution for a single layer is enabled by the periodic arrangements of the four-site unit cell shown in Fig. 1. Such a unit-cell consists of two areas with the conductivity $\kappa_A(\mathbf{r})$ and two areas with $\kappa_B(\mathbf{r})$, which are alternatively connected with each other. For each site, the corresponding conductivity satisfies centrosymmetric distribution in their local coordinates, whose center is $\mathrm{O}_{\mathrm{loc}}^{n_{index}}$ and $n_{index} = \left\lceil \frac{\theta}{\frac{\pi}{2}} \right\rceil$ denotes the serial number of related quadrant ranging from 1 to 4. Here, $\left\lceil \frac{\theta}{\frac{\pi}{2}} \right\rceil$ is a celling function in mathematics, which maps times between the azimuth of a selected point and $\frac{\pi}{2}$ to the least integer greater than the real number of $\frac{\theta}{\frac{\pi}{2}}$. Then, their conductivity can be described as the spatial-dependent expressions in their local coordinates, i.e., $\kappa_A(\mathbf{r}) = \kappa_A \frac{r_{loc,A}}{r_{max}}$ and $\kappa_B(\mathbf{r}) = \kappa_B \frac{r_{loc,B}}{r_{max}}$. $r_{loc,A}$ and $r_{loc,B}$ respectively denote the radial components in their local coordinates centered on $\mathrm{O}_{\mathrm{loc}}^{n_{index}}$, while r_{max} is the largest value of each site equaling to $\frac{l}{\sqrt{2}}$ based on the geometrical characteristics (Fig. S1**a**). In order to simplify the description for creating the superlattice with periodic unit-cell and Bloch theorem, we adopt a global system to express the conductivity distributions in each unit cell. In this case, the conductivity at the center O of the global system is $\kappa_0 = \frac{\kappa_A + \kappa_B}{2}$. In this case, the conductivities at the centers of corresponding local coordinates $\mathrm{O}_{\mathrm{loc}}^{n_{index}}$ can be written with κ_0 as $\kappa_A = \kappa_0 + \frac{\kappa_A - \kappa_B}{2}$ and $\kappa_B = \kappa_0 - \frac{\kappa_A - \kappa_B}{2}$. Considering the spatial characteristics and arrangements, the $\kappa_A(\mathbf{r})$ and $\kappa_B(\mathbf{r})$ are respectively set in the 2nd/4th and 1st/3rd quadrants. That is, the sign of the term $\frac{\kappa_A - \kappa_B}{2}$ in κ_A and κ_B is consistent with $\tan\theta$ in related quadrants depending on the azimuth. Then, we can obtain the amplitude with κ_0 in the global system

$$\kappa_{A/B} = \kappa_0 + \frac{\kappa_A - \kappa_B}{2} \mathrm{sgn}\left(\frac{\tan\theta}{|\tan\theta|}\right). \tag{S1}$$

Since we only need the sign information, we take the function of $\mathrm{sgn}\left(\frac{\tan\theta}{|\tan\theta|}\right)$ to indicate site A or B. Upon the local conductivity $\kappa_A(\mathbf{r}) = \kappa_A \frac{r_{loc,A}}{r_{max}}$ and $\kappa_B(\mathbf{r}) = \kappa_B \frac{r_{loc,B}}{r_{max}}$, we then transform the spatial character $\frac{r_{A/B}}{r_{max}}$ to the global system. Note that, the local conductivity at a selected point only depends on the scale parameter related to the distance ($r_{max} = \frac{l}{\sqrt{2}}$) between global and local origins (O and $\mathrm{O}_{\mathrm{loc}}^{n_{index}}$). In this case, we need to express $r_{loc,A/B}$ with the global coordinate. Considering the rotational symmetry of the spatial characters of each site, we take site A in the second quadrant as a

representation (Figs. S1**b** and **c**), while $n_{index} = 2$ in this site A. Since we take the distance $r_{max} = \frac{l}{\sqrt{2}}$ (length of line $\mathrm{OO}_{\mathrm{loc}}^{2}$) and the included angle $(2n_{index} - 1)\frac{\pi}{4} = \frac{3\pi}{4}$ as reference, two types of $r_{loc,A}$ can be defined with the real positions of the selected points based on the diagonal line (black dashed line) perpendicular to line $\mathrm{OO}_{\mathrm{loc}}^{n_{index}}$, including 1. The position (red dot) is upper than the black dashed line (Fig. S1**b**); 2. The position (red dot) is lower than the black dashed line (Fig. S1**c**). The length of line OA between the origin of the global coordinate and the selected point is r, while l_1 and l_2 are the lengths of vertical line to OA and the line OA'.

For the first case (Fig. S1**b**), $r_{loc,A} = \sqrt{l_1^2 + (r - l_2)^2}$. The lengths of l_1 and l_2 can be determined in the right triangle $\mathrm{O}_{\mathrm{loc}}^{n_{index}}AA'$ with the distances $r - l_2$ between points A and A', l_1 and the included angle $\theta - \frac{3\pi}{4}$. That is, $l_1 = r_{max}\sin\left(\theta - \frac{3\pi}{4}\right)$ and $l_2 = r_{max}\cos\left(\theta - \frac{3\pi}{4}\right)$, which further result in

$$r_{loc,A} = \sqrt{\left(r - \frac{l}{\sqrt{2}}\right)^2 + \sqrt{2}rl - \sqrt{2}rl\cos\left(\theta - \frac{3\pi}{4}\right)}. \tag{S2}$$

Taking such relation to $\kappa_A(\mathbf{r}) = \kappa_A\frac{r_{loc,A}}{r_{max}}$, we obtain $\kappa_A(\mathbf{r}) = \left(\frac{|\kappa_A+\kappa_B|}{2} + \frac{\kappa_A-\kappa_B}{2}\right)\frac{\sqrt{\left(r-\frac{l}{\sqrt{2}}\right)^2+\sqrt{2}rl-\sqrt{2}rl\cos\left(\theta-\frac{3\pi}{4}\right)}}{\frac{l}{\sqrt{2}}}$ in . Though the changing position of point A leads to the changing length of line AA' as $(l_2 - r)$ in the second case, l_1 and l_2 still maintain the same values as the first case due to the similar geometrical property. Thus, the distance between points A and $\mathrm{O}_{\mathrm{loc}}^{n_{index}}$ also maintain the same value as the first case, i.e., $r_{loc,A} = \sqrt{l_1^2 + (l_2 - r)^2}$. That is, we have the consistent form for describing the conductivity distribution in both upper and lower areas than the diagonal line (black dashed line), i.e., $\kappa_A(\mathbf{r}) = \left(\frac{|\kappa_A+\kappa_B|}{2} + \frac{\kappa_A-\kappa_B}{2}\right)\frac{\sqrt{\left(r-\frac{l}{\sqrt{2}}\right)^2+\sqrt{2}rl-\sqrt{2}rl\cos\left(\theta-\frac{3\pi}{4}\right)}}{\frac{l}{\sqrt{2}}}$. Due to the similar local geometrical property and rotational symmetry of the global system, we can achieve the general expression of the conductivity distribution in the region of the four-site unit-cell as

$$\kappa(\mathbf{r}) = \left(\frac{|\kappa_A+\kappa_B|}{2} + \frac{\kappa_A-\kappa_B}{2}\mathrm{sgn}\left(\frac{\tan\theta}{|\tan\theta|}\right)\right)\frac{\sqrt{\left(r-\frac{l}{\sqrt{2}}\right)^2+\sqrt{2}rl-\sqrt{2}rl\cos\left(\theta-(2n_{index}-1)\frac{\pi}{4}\right)}}{\frac{l}{\sqrt{2}}}. \tag{S3}$$

In the theoretical calculations in Fig. 2 of the main content, the thermal conductivities of neighboring sites within a single layer are assigned as $\kappa_A = 10\kappa_{ref}$ and $\kappa_B = 0.1\kappa_{ref}$, and $\kappa_{ref} = 1$ $\mathrm{W{\cdot}m^{-1}{\cdot}K^{-1}}$ serves as the reference thermal

conductivity.

2. Governing function of the conductive moiré superlattice

The properties of the heat transfer process within the conductive moiré superlattice are enabled by the heat exchanges of the bilayer systems at the two interfaces. That is, such behaviors at different twisted angles are determined by the linear superposition of thermal interactions of mismatched sites in each monolayer. Here, we start with a general thermal process in a monolayer. Upon the periodic configurations of the four-site unit cells, inhomogeneous conductive couplings occur both along the *x* and *y* directions, while no couplings exist along *z* direction. The general expression considering spatial-dependent conductivity can be then described as

$$\nabla \cdot \left(\kappa(\mathbf{r})\nabla T(\mathbf{r},t)\right) - \rho c \frac{\partial T(\mathbf{r},t)}{\partial t} = 0, \tag{S4}$$

where $\mathbf{r} = (r\cos\theta, r\sin\theta, 0) = (x, y, 0)$ denotes the coordinate of the global system. Taking account of the conductivity distribution of a unit-cell and the Bloch theorem, the periodically inhomogeneous conductivity of the monolayer can be then denoted as $\kappa(\mathbf{r}) = \left(\frac{|\kappa_A+\kappa_B|}{2} + \frac{\kappa_A-\kappa_B}{2}\mathrm{sgn}\left(\frac{\tan\theta}{|\tan\theta|}\right)\right)\frac{\sqrt{\left(r-\frac{l}{\sqrt{2}}\right)^2+\sqrt{2}rl-\sqrt{2}rl\cos\left(\theta-(2n_{index}-1)\frac{\pi}{4}\right)}}{\frac{l}{\sqrt{2}}}e^{i(k_x+k_y)}$. Note that, $\mathbf{k} = (k_x, k_y, 0)$ is the effective momentum space in the monolayer for generating the target moiré superlattice at a tailored twist angle. The expressions of $k_x = \frac{2\pi}{l_s}$ and $k_y = \frac{2\pi}{l_s}$ indicate the effective wavenumbers, while l_s is integer times of the site length l for counting the quantity of the involved sites in generating the moiré superlattice following Pythagorean theorem. In order to discover the thermal evolution, we consider an incident temperature field which can be separated in both the spatial and time domain as the initial boundary condition $T(\mathbf{r},t) = \psi(\mathbf{r})U(t)$. Due to the in-plane spatial-dependent conductivity, the conductive terms can be then expanded as

$$\nabla \cdot \left(\kappa(\mathbf{r}) \cdot \nabla T(\mathbf{r},t)\right) \to \left(\left(\kappa_{rr}\frac{\partial^2\psi(\mathbf{r})}{\partial r^2} + \kappa_{r\theta}\frac{\partial^2\psi(\mathbf{r})}{\partial r\partial\theta} + \frac{\kappa_{\theta\theta}}{r}\frac{\partial^2\psi(\mathbf{r})}{\partial\theta^2} + \frac{\kappa_{\theta r}}{r}\frac{\partial^2\psi(\mathbf{r})}{\partial r\partial\theta}\right) + \left(\frac{\partial\kappa(\mathbf{r})}{\partial r}\frac{\partial\psi(\mathbf{r})}{\partial r} + \frac{1}{r}\frac{\partial\kappa(\mathbf{r})}{\partial\theta}\frac{\partial\psi(\mathbf{r})}{\partial\theta}\right)\right)U(t). \tag{S5}$$

Two first-order terms of $\frac{\partial\kappa(\mathbf{r})}{\partial r}\frac{\partial\psi(\mathbf{r})}{\partial r}$ and $\frac{1}{r}\frac{\partial\kappa(\mathbf{r})}{\partial\theta}\frac{\partial\psi(\mathbf{r})}{\partial\theta}$ occur and induce two potential fields $\frac{\partial\kappa(\mathbf{r})}{\partial r}$ and $\frac{1}{r}\frac{\partial\kappa(\mathbf{r})}{\partial\theta}$ to drive heat flux, which act as the role of effective advections in corresponding directional components. Further taking Eq. (S5) to Eq. (S4), we observe

$$\frac{1}{\psi(\mathbf{r})}\left(\left(\kappa_{rr}\frac{\partial^2\psi(\mathbf{r})}{\partial r^2}+\kappa_{r\theta}\frac{\partial^2\psi(\mathbf{r})}{\partial r\partial\theta}+\frac{\kappa_{\theta\theta}}{r}\frac{\partial^2\psi(\mathbf{r})}{\partial\theta^2}+\frac{\kappa_{\theta r}}{r}\frac{\partial^2\psi(\mathbf{r})}{\partial r\partial\theta}\right)+\left(\frac{\partial\kappa(\mathbf{r})}{\partial r}\frac{\partial\psi(\mathbf{r})}{\partial r}+\frac{1}{r}\frac{\partial\kappa(\mathbf{r})}{\partial\theta}\frac{\partial\psi(\mathbf{r})}{\partial\theta}\right)\right)=\rho c\frac{1}{U(t)}\frac{\partial U(t)}{\partial t}=a. \quad \text{(S6)}$$

In Eq. (S6), a is a separation constant, which stands for the net energy after heat exchange of the system, i.e., eigenenergy. For generalization and representation, we take a plane-wave function to act as the role of spatial-temporal temperature at the interface, i.e., $T(\mathbf{r},t)=\psi(\mathbf{r})U(t)=Ae^{i(\mathbf{k}\cdot\mathbf{r}-\omega t)}$. In this case, we have $a=i(\mathbf{k}\cdot\mathbf{k})D(\mathbf{r})+\mathbf{k}\cdot\nabla D(\mathbf{r})$, whose real and imaginary parts respectively denote the drift components caused by spatial conductivity and in-situ conductive (decay) components. Taking the heat exchange energy a in Eq. (S6), the following relation independent of time (steady state) can be identified:

$$\left(\left(\kappa_{rr}\frac{\partial^2}{\partial r^2}+\kappa_{r\theta}\frac{\partial^2}{\partial r\partial\theta}+\frac{\kappa_{\theta\theta}}{r}\frac{\partial^2}{\partial\theta^2}+\frac{\kappa_{\theta r}}{r}\frac{\partial^2}{\partial r\partial\theta}\right)+\left(\frac{\partial\kappa(\mathbf{r})}{\partial r}\frac{\partial}{\partial r}+\frac{1}{r}\frac{\partial\kappa(\mathbf{r})}{\partial\theta}\frac{\partial}{\partial\theta}\right)+\rho ca\right)\psi(\mathbf{r})=0. \quad \text{(S7)}$$

In order to create the conductive moiré superlattice, we further adopt another monolayer with the same conductivity distribution, and further stack two such layers with a twisted angle φ. In this case, a rotational matrix $R(\varphi)=\begin{pmatrix}\cos\varphi & -\sin\varphi & 0\\ \sin\varphi & \cos\varphi & 0\\ 0 & 0 & 1\end{pmatrix}$ should be introduced to maintain the same coordinates of the stacking layers, which further result in the effective momentum space $\mathbf{k}'=(k_x,k_y,k_z)R(\varphi)=(k_x\cos\varphi-k_y\sin\varphi\,,k_x\sin\varphi+k_y\cos\varphi\,,k_z)$ of the twisted layer. Considering the translational symmetry and periodicity, the conductivity distributions in the twisted layer can be then described as

$$\kappa(\mathbf{r}')=\left(\frac{|\kappa_A+\kappa_B|}{2}+\frac{\kappa_A-\kappa_B}{2}\operatorname{sgn}\left(\frac{\tan\theta}{|\tan\theta|}\right)\right)\frac{\sqrt{\left(r-\frac{l}{\sqrt{2}}\right)^2+\sqrt{2}rl-\sqrt{2}rl\cos\left(\theta-(2n_{index}-1)\frac{\pi}{4}\right)}}{\frac{l}{\sqrt{2}}}e^{i(k_x'+k_y')}. \quad \text{(S8)}$$

Taking Eq. (S8) into Eq. (S4) of the twisted layer under the same plane-wave function $T(\mathbf{r},t)=\psi(\mathbf{r})U(t)=Ae^{i(\mathbf{k}'\cdot\mathbf{r}'-\omega' t)}$, we have the following relationship

$$\frac{1}{\psi(\mathbf{r})}\left(\left(\kappa_{r'r'}\frac{\partial^2\psi(\mathbf{r})}{\partial r^2}+\kappa_{r'\theta'}\frac{\partial^2\psi(\mathbf{r})}{\partial r\partial\theta}+\frac{\kappa_{\theta'\theta'}}{r}\frac{\partial^2\psi(\mathbf{r})}{\partial\theta^2}+\frac{\kappa_{\theta'r'}}{r}\frac{\partial^2\psi(\mathbf{r})}{\partial r\partial\theta}\right)+\left(\frac{\partial\kappa(\mathbf{r}')}{\partial r}\frac{\partial\psi(\mathbf{r})}{\partial r}+\frac{1}{r}\frac{\partial\kappa(\mathbf{r}')}{\partial\theta}\frac{\partial\psi(\mathbf{r})}{\partial\theta}\right)\right)=\rho c\frac{1}{U(t)}\frac{\partial U(t)}{\partial t}=a_r. \quad \text{(S9)}$$

In Eq. (S9), $a_r=i(\mathbf{k}'\cdot\mathbf{k}')D(\mathbf{r}')+\mathbf{k}'\cdot\nabla D(\mathbf{r}')$ is a separation constant in the twisted layer representing the net energy (eigenenergy) after heat exchange of the system. This further leads to the energy equation at steady state of the twisted layer as

$$\left(\left(\kappa_{r'r'}\frac{\partial^2}{\partial r^2}+\kappa_{r'\theta'}\frac{\partial^2}{\partial r\partial\theta}+\frac{\kappa_{\theta'\theta'}}{r}\frac{\partial^2}{\partial\theta^2}+\frac{\kappa_{\theta'r'}}{r}\frac{\partial^2}{\partial r\partial\theta}\right)+\left(\frac{\partial\kappa(\mathbf{r}')}{\partial r}\frac{\partial}{\partial r}+\frac{1}{r}\frac{\partial\kappa(\mathbf{r}')}{\partial\theta}\frac{\partial}{\partial\theta}\right)+\rho c a_r\right)\psi(\mathbf{r})=0. \tag{S10}$$

Then, the energy equation of the conductive moiré superlattice at the interface after stacking can be observed by the superposition of Eqs. (S7) and (S10)

$$\left(\begin{array}{c}\left(\left(\kappa_{rr}+\kappa_{r'r'}\right)\frac{\partial^2}{\partial r^2}+\left(\kappa_{r\theta}+\kappa_{r'\theta'}\right)\frac{\partial^2}{\partial r\partial\theta}+\frac{\left(\kappa_{\theta\theta}+\kappa_{\theta'\theta'}\right)}{r}\frac{\partial^2}{\partial\theta^2}+\frac{\left(\kappa_{\theta r}+\kappa_{\theta'r'}\right)}{r}\frac{\partial^2}{\partial r\partial\theta}\right)\\+\left(\left(\frac{\partial\kappa(\mathbf{r})}{\partial r}+\frac{\partial\kappa(\mathbf{r}')}{\partial r}\right)\frac{\partial}{\partial r}+\frac{1}{r}\left(\frac{\partial\kappa(\mathbf{r})}{\partial\theta}+\frac{\partial\kappa(\mathbf{r}')}{\partial\theta}\right)\frac{\partial}{\partial\theta}\right)+\rho c(a+a_r)\end{array}\right)\psi(\mathbf{r})=0. \tag{S11}$$

In order to discover the property and temperature field evolution of the conductive moiré superlattice, a vertical heat flux along z-direction should be adopted as an incident wave to motivate the behaviors at specific twisted angles. In that case, we should maintain an extremely small thickness on each layer along the vertical heat flux to avoid the thermal interactions along z-direction. Thus, we make the thin plate of each layer with the thickness of h_p = 1 mm to enable the far smaller thermal conduction distances than the ones in the x-y plane. This setup leads to the much weaker thermal exchanges with near-zero temperature difference along z-direction, i.e., $\nabla_z T \to \partial_z T \to 0$, $\nabla_z^2 T \to 0$ and $\nabla_z^2 T \ll \nabla_{r-\theta}(\nabla_{r-\theta} T)$ at the interface, and further make the system satisfy a slowly varying approximation in the thermal evolution process under the vertical heat flux at steady state. For representation, we take $\psi(\mathbf{r}) = m(\mathbf{r})e^{ik_z z}$. Then, Eq. (S11) can be rewritten as below

$$\left(\begin{array}{c}\left(\left(\kappa_{rr}+\kappa_{r'r'}\right)\frac{\partial^2}{\partial r^2}+\left(\kappa_{r\theta}+\kappa_{r'\theta'}\right)\frac{\partial^2}{\partial r\partial\theta}+\frac{\left(\kappa_{\theta\theta}+\kappa_{\theta'\theta'}\right)}{r}\frac{\partial^2}{\partial\theta^2}+\frac{\left(\kappa_{\theta r}+\kappa_{\theta'r'}\right)}{r}\frac{\partial^2}{\partial r\partial\theta}\right)\\+\left(\left(\frac{\partial\kappa(\mathbf{r})}{\partial r}+\frac{\partial\kappa(\mathbf{r}')}{\partial r}\right)\frac{\partial}{\partial r}+\frac{1}{r}\left(\frac{\partial\kappa(\mathbf{r})}{\partial\theta}+\frac{\partial\kappa(\mathbf{r}')}{\partial\theta}\right)\frac{\partial}{\partial\theta}\right)+\rho c(a+a_r)\end{array}\right)m(\mathbf{r})e^{ik_z z}=0. \tag{S12}$$

Here, $\frac{\partial\psi}{\partial z}=\left(\frac{\partial m}{\partial z}+ik_z m\right)e^{ik_z z}$ and $\frac{\partial^2\psi}{\partial z^2}=\left(\frac{\partial^2 m}{\partial z^2}+2ik_z\frac{\partial m}{\partial z}-k_z^2 m\right)e^{ik_z z}$. For simplification, we further take the length along z-direction (total thickness of the two conductive layers) as the effective wavelength λ_z, and $k_z=\frac{2\pi}{\lambda_z}$ defines the effective wavenumber for the incident wave. Owing to the slowly varying function in z-direction, we have $\left|\frac{\partial^2 m}{\partial z^2}\right| \ll \left|k\frac{\partial m}{\partial z}\right|$. Taking these relations to Eq. (S12), we can obtain the following equation to describe the moiré property at the interface

$$\left(\left(\kappa_{rr}+\kappa_{r'r'}\right)\frac{\partial^2}{\partial r^2}+\left(\kappa_{r\theta}+\kappa_{r'\theta'}\right)\frac{\partial^2}{\partial r\partial\theta}+\frac{\left(\kappa_{\theta\theta}+\kappa_{\theta'\theta'}\right)}{r}\frac{\partial^2}{\partial\theta^2}+\frac{\left(\kappa_{\theta r}+\kappa_{\theta'r'}\right)}{r}\frac{\partial^2}{\partial r\partial\theta}\right)\psi+\rho c2ik_z\partial_z\psi+\left(\nabla\cdot\kappa(\mathbf{r})+\nabla\cdot\kappa(\mathbf{r}')\right)\cdot$$
$$\nabla_{r-\theta}\psi+\rho c\left(a+a_r+D_z k_z^2\right)\psi=0.$$

The term $D_z k_z^2 \psi$ can be be further expressed as a function of the thermal energy component along z-direction based on Eqs. (S6) and (S9), and $D_z = \frac{\kappa_{zz}+\kappa_{z'z'}}{\rho c}$ in the stacking system. Thus, we have $\left(\nabla_z^2 + \frac{1}{D} a_z\right)\psi = 0$. Given the assumption of smaller out-of-plane thermal processes $\nabla_z^2 T \ll \nabla_{r-\theta}(\nabla_{r-\theta} T)$, the component $\nabla_z^2 \psi$ can be neglected. Upon the above implementation, we have

$$ik_z \frac{\partial \psi}{\partial z} = -\frac{\left(\left(\kappa_{rr}+\kappa_{r'r'}\right)\frac{\partial^2}{\partial r^2}+\left(\kappa_{r\theta}+\kappa_{r'\theta'}\right)\frac{\partial^2}{\partial r\partial\theta}+\frac{\left(\kappa_{\theta\theta}+\kappa_{\theta'\theta'}\right)}{r}\frac{\partial^2}{\partial\theta^2}+\frac{\left(\kappa_{\theta r}+\kappa_{\theta' r'}\right)}{r}\frac{\partial^2}{\partial r\partial\theta}\right)}{\rho c} - \frac{\left(\nabla\cdot\kappa(\mathbf{r})+\nabla\cdot\kappa(\mathbf{r}')\right)\cdot\nabla_{r-\theta}\psi}{\rho c} + (a+a_r)\psi \quad \text{(S13)}$$

Equation (S13) indicates the general thermal process under vertical flux inputs in the bilayer system. To examine the energy conversion at the stacked interface of the fixed and rotated layers. Considering the nearest neighboring sites and corresponding couplings in a unit cell of the emerging superlattice, Eq. (S13) can be written in a form of effective Hamiltonian

$$i\frac{\partial \psi}{\partial z} = H_{\text{moire}}\psi, \quad \text{(S14)}$$

$$H_{\text{moire}} = -\frac{\left(\left(\kappa_{rr}+\kappa_{r'r'}\right)\frac{\partial^2}{\partial r^2}+\left(\kappa_{r\theta}+\kappa_{r'\theta'}\right)\frac{\partial^2}{\partial r\partial\theta}+\frac{\left(\kappa_{\theta\theta}+\kappa_{\theta'\theta'}\right)}{r}\frac{\partial^2}{\partial\theta^2}+\frac{\left(\kappa_{\theta r}+\kappa_{\theta' r'}\right)}{r}\frac{\partial^2}{\partial r\partial\theta}\right)}{\rho c k_z} - \frac{\left(\nabla\cdot\kappa(\mathbf{r})+\nabla\cdot\kappa(\mathbf{r}')\right)\cdot\nabla_{r-\theta}}{\rho c k_z} + \frac{(a+a_r)}{k_z}. \quad \text{(S15)}$$

Considering the anisotropic conductivity in the superlattice, we can decouple the energy components in corresponding directions to express the heat exchanges. In this case, a 4×4 matrix is available for denoting the in-plane energy and present the effective Hamiltonian for a unit cell of the moiré superlattice

$$H_{moire,unit} = -i\begin{bmatrix} \frac{\kappa_{rr}+\kappa_{r'r'}}{\rho c k_z} - i\left(\nabla\cdot\kappa(\mathbf{r})+\nabla\cdot\kappa(\mathbf{r}')\right)_r & \frac{\kappa_{r\theta}+\kappa_{r'\theta'}}{\rho c k_z} - i\frac{(a+a_r)}{k_z}e^{ik_{x,moire}l_{moire}} & 0 & -i\frac{(a+a_r)}{k_z}e^{-ik_{y,moire}l_{moire}} \\ \frac{\left(\kappa_{\theta r}+\kappa_{\theta' r'}\right)}{r\rho c k_z} - i\frac{(a+a_r)}{k_z}e^{-ik_{x,moire}l_{moire}} & \frac{\left(\kappa_{\theta\theta}+\kappa_{\theta'\theta'}\right)}{r\rho c k_z} - i\left(\nabla\cdot\kappa(\mathbf{r})+\nabla\cdot\kappa(\mathbf{r}')\right)_\theta & -i\frac{(a+a_r)}{k_z}e^{-ik_{y,moire}l_{moire}} & 0 \\ 0 & -i\frac{(a+a_r)}{k_z}e^{ik_{y,moire}l_{moire}} & \frac{\kappa_{rr}+\kappa_{r'r'}}{\rho c k_z} - i\left(\nabla\cdot\kappa(\mathbf{r})+\nabla\cdot\kappa(\mathbf{r}')\right)_r & \frac{\kappa_{r\theta}+\kappa_{r'\theta'}}{\rho c k_z} - i\frac{(a+a_r)}{k_z}e^{-ik_{x,moire}l_{moire}} \\ -i\frac{(a+a_r)}{k_z}e^{ik_{y,moire}l_{moire}} & 0 & \frac{\left(\kappa_{\theta r}+\kappa_{\theta' r'}\right)}{r\rho c k_z} - i\frac{(a+a_r)}{k_z}e^{ik_{x,moire}l_{moire}} & \frac{\left(\kappa_{\theta\theta}+\kappa_{\theta'\theta'}\right)}{r\rho c k_z} - i\left(\nabla\cdot\kappa(\mathbf{r})+\nabla\cdot\kappa(\mathbf{r}')\right)_\theta \end{bmatrix}, \quad \text{(S16)}$$

where, l_{moire} is the lattice constant of the moiré superlattice, which can be obtained with l_s following Pythagorean theorem.

3. Effective wavevectors of the conductive moiré superlattice

The stacking bilayers lead to a new spatial period in conductivity distributions for generating moiré superlattice, i.e., $\kappa(\mathbf{r}) + \kappa(\mathbf{r}') \to \kappa(\mathbf{r})\left(e^{i\mathbf{k}\cdot\mathbf{r}_{\text{moire}}} + e^{i\mathbf{k}'\cdot\mathbf{r}_{\text{moire}}}\right)$, $\mathbf{r}_{\text{moire}}$ represents the coordinate of the emerging moiré pattern.. In this

spatial characteristic, it satisfies the form of two plane wave superpositions, where $\kappa(\mathbf{r})$ plays the role of periodic conductivity with the same periodicity as the lattice, while $e^{i(k_x+k_y)}$ and $e^{i(k_x'+k_y')}$ are the two plane waves. For simplification, we make $A = k_x x + k_y y$ and $B = k_x' x' + k_y' y' = k_x x(\cos\varphi + \sin\varphi) + k_y y(\cos\varphi - \sin\varphi)$.

Following the principle of wave superposition, we have

$$\kappa(\mathbf{r})\left(e^{i(k_x x+k_y y)} + e^{i(k_x' x'+k_y' y')}\right) \to \kappa(\mathbf{r})(e^{iA} + e^{iB}) = \kappa(\mathbf{r}) e^{i\frac{A+B}{2}}\left(e^{i\frac{A-B}{2}} + e^{-i\frac{A-B}{2}}\right). \quad \text{(S17)}$$

Further combining the terms using the identity for the sum of exponentials, Eq. (S17) can be rewritten as

$$\kappa(\mathbf{r}_{\text{moire}}) = 2\kappa(\mathbf{r}) e^{i\frac{k_x x(1+\cos\varphi+\sin\varphi)+k_y y(1+\cos\varphi-\sin\varphi)}{2}} \cos\left(\frac{k_x x(1-\cos\varphi-\sin\varphi)+k_y y(1-\cos\varphi+\sin\varphi)}{2}\right) = 2\kappa(\mathbf{r}) e^{i\frac{\mathbf{k}+\mathbf{k}'}{2}\mathbf{r}_{\text{moire}}} \cos\left(\frac{\mathbf{k}-\mathbf{k}'}{2}\cdot\mathbf{r}_{\text{moire}}\right). \quad \text{(S18)}$$

The emerging conductivity indicated by Eq. (S18) possesses two types of effective wavevectors, including the global wavevectors for presenting periodic function of the emerging moiré superlattice $\mathbf{k}_{\text{moire}} = \frac{\mathbf{k}+\mathbf{k}'}{2}$, and an effective wavevector $\mathbf{k}_{\text{mod}} = \frac{\mathbf{k}-\mathbf{k}'}{2}$ caused by the difference of the superposed two wavevectors for modulating the interior profile of moiré pattern.

The global wavevector defines the general periodicity of the moiré superlattice, which also implies the matching frequency for motivating the moiré property at tailored twisted angles, i.e., the wavenumbers involved in the superlattice. In Fig. 1**d** of the main content, the normalized wavenumbers caused by $\mathbf{k}_{\text{moire}}$ maintain approximate symmetry centered on the twisted angle of $\frac{\pi}{4}$, though slight deviations occur and lead to smaller values ranging from $\frac{\pi}{4}$ to $\frac{\pi}{2}$ than the corresponding ones between 0 to $\frac{\pi}{4}$. Such differences result in few changes in lattice scales of the unit cells at the symmetric twist angles φ and $\frac{\pi}{2} - \varphi$ (Figs. S2**a** and **b**).

The second effective wavevector $\mathbf{k}_{\text{mod}}$ mostly manipulates the property in one unit cell at a twisted angle. It shows apparently different values (wavenumbers) at the symmetric twist angles φ and $\frac{\pi}{2} - \varphi$ as plotted in Fig. 1**d**. Smaller values occur at the twisted angles ranging from 0 to $\frac{\pi}{4}$ than their symmetrical counterparts between $\frac{\pi}{4}$, to $\frac{\pi}{2}$. That is, fewer wavenumbers could be involved in each unit cell in contrast to the ones enabled by the twisted angles larger than $\frac{\pi}{4}$, thus leading to stronger obstructions for the heat flux propagation at the interface and potential localizations in temperature

field with larger temperature differences. Such behaviors are induced by the observably different pattern details in the conductive distributions at the symmetric twist angles φ and $\frac{\pi}{2}-\varphi$, which further result in the different anisotropic degrees as shown in Fig. 2**e**. Here, the anisotropic degree in Fig. 2**e** of the main content is defined by $\frac{\sum\frac{|\kappa_{r,moire}-\kappa_0|}{\kappa_0}+\sum\frac{|\kappa_{\theta,moire}-\kappa_0|}{\kappa_0}}{2N}$, where N denotes the quantity of the selected points in the target superlattices. The numerator presents the sum of the deflected ratios of the directional conductive components, thus a term "2" is adopted in the denominator to solve the average value along the two directions. Notably, some pioneering reports regarding the commensurate and incommensurate moiré patterns have neglected the differences between directional wavevectors of the emerging superlattice after superposing the two plane-wave components, thus only symmetric lattice constants and effective wavenumbers $|\mathbf{k}_{\mathrm{ref}}|$ centered on $\pi/4$ are obtained as shown in the right-inset of Fig. 1**e** of the main content.

It is worth noting that the translational axis (base vectors) of the emerging moiré pattern could reveal a deflection β related to the coordinate of the initial layer in the *x*-*y* plane. Following the principle of wave superposition, we can identify the expression with the wavevectors of $\mathbf{k}_{\mathrm{moire}}$ for the superlattice and the $\mathbf{k}$ for the initial layer as

$$\beta=\arccos\left(\frac{\mathbf{k}_{moire}\cdot\mathbf{k}}{|\mathbf{k}_{moire}||\mathbf{k}|}\right)=\frac{\sqrt{2}}{2}\frac{k_x^2(1+\cos\varphi+\sin\varphi)+k_y^2(1+\cos\varphi-\sin\varphi)}{\sqrt{k_x^2+k_y^2}\sqrt{k_x^2(1+\cos\varphi+\sin\varphi)+k_y^2(1+\cos\varphi-\sin\varphi)}}. \tag{S19}$$

Due to the square lattice of the considered cases, the same effective wavenumbers of k_x and k_y lead to $\beta=\arccos\left(\frac{\mathbf{k}_{moire}\cdot\mathbf{k}}{|\mathbf{k}_{moire}||\mathbf{k}|}\right)=\frac{\varphi}{2}$ in the above cases. That is, the deflected degrees of the superlattice are half of the twisted angles. When the effective wavenumbers of k_x and k_y are inconsistent, the value of β depends on the ratio of $\frac{k_x}{k_y}$ and the twisted angle φ (Fig. S2**c**).

4. Non-dimensional description of the conductive moiré superlattice

The effective lattice constants dramatically change with the twisted angles. For observing the general thermal property without scale effects, we adopt a non-dimensional analysis with Eq. (S6). Since such a moiré superlattice is created by stacking two independent conductive layers with tailored conductivity distributions, we select the unit-cell as the reference model from one conductive layer, whose parameters possess the same identical geometry and

average conductivity for each unit cell. ($l_{ref} = 10\,mm$ and $\kappa_{ref} = \kappa_0 = 5\ \mathrm{W \cdot m^{-1} \cdot K^{-1}}$). In that case, the reference in-plane wavevector is $\mathbf{k}_{ref} = \left(\frac{2\pi}{l_{ref}}, \frac{2\pi}{l_{ref}}\right)$ For simplification, we take $t_{ref} = 10000\ s$ for enabling steady state as the reference time and $\psi_{ref} = \Delta T$ as the reference temperature field. Note that, ΔT denotes the difference between the peak and valley values of the imposed temperature wave. The reference heat exchange can be then selected as $a_{ref} = i\left(\mathbf{k}_{ref} \cdot \mathbf{k}_{ref}\right)\frac{\boldsymbol{\kappa}(\mathbf{r})}{\rho c} + \mathbf{k}_{ref} \cdot \frac{\boldsymbol{\kappa}(\mathbf{r})}{\rho c}$ In that case, the non-dimensional parameters can be defined as $r^* = \frac{r}{l_{ref}}$, $\theta^* = \frac{\theta}{\theta_{ref}}$, $l^* = \frac{l_{moire}}{l_{ref}}$, $\boldsymbol{\kappa}^* = \frac{\boldsymbol{\kappa}}{\kappa_{ref}}$ $\boldsymbol{\nabla}^* = l_{ref}\boldsymbol{\nabla}$, $\psi^* = \frac{\psi}{\psi_{ref}}$, $a^* = \frac{a}{a_{ref}}$, $\mathbf{k}^* = \frac{\mathbf{k}_{moire}}{\mathbf{k}_{ref}}$, $\mathbf{D}^* = \frac{\mathbf{D}_{moire}}{D_{ref}} = \frac{\boldsymbol{\kappa}}{\kappa_{ref}}$ and $t^* = \frac{t}{t_{ref}}$. Taking these non-dimensional parameters into Eq. (S6), we have

$$\left(\kappa^*_{rr}\frac{\partial^2\psi^*}{\partial r^{*2}} + \kappa^*_{r\theta}\frac{\partial^2\psi^*}{\partial r^*\partial\theta^*} + \frac{\kappa^*_{\theta\theta}}{r^*}\frac{\partial^2\psi^*}{\partial\theta^{*2}} + \frac{\kappa^*_{\theta r}}{r^*}\frac{\partial^2\psi^*}{\partial r^*\partial\theta^*}\right) + \left(\boldsymbol{\nabla}^*\boldsymbol{\kappa}^*\right)\cdot\left(\boldsymbol{\nabla}^*\psi^*\right) - \frac{1}{\mathrm{Fo}}\frac{\partial\psi^*}{\partial t^*} = a^*, \tag{S20}$$

where, $\langle \mathrm{Fo} \rangle = \frac{\langle \mathbf{D}^* \rangle t^*}{r^*}$ is the Fourier number for evaluating the ratio between the propagation of heat transfer and thermal storage in a finite conductive system, and $\langle ... \rangle$ denotes a 2D spatial average at the interface. Note that, the first-order term $\left(\boldsymbol{\nabla}^*\boldsymbol{\kappa}^*\right)\cdot\left(\boldsymbol{\nabla}^*\psi^*\right)$ caused by the anisotropic conductivity distributions provides a convection-like drift $\left(\boldsymbol{\nabla}^*\boldsymbol{\kappa}^*\right)$ in temperature fields, thus, we could treat it as an effective velocity in the current system, i.e., $\mathbf{v}^*_{\boldsymbol{eff}} = \boldsymbol{\nabla}^*\boldsymbol{\kappa}^*$. Thus, an effective Péclet number (Pe) can be also indicated as $\langle \mathrm{Pe} \rangle = \frac{\langle \mathbf{v}^*_{\boldsymbol{eff}} \rangle r^*}{\langle \mathbf{D}^* \rangle}$ for presenting the energy ratio between the effective convection and in-situ conduction. Such an effective $\langle \mathrm{Pe} \rangle$ maintains a relation with the characteristic length r^*, and leads to $\frac{r^*}{\langle \mathrm{Pe} \rangle} = \frac{\langle \mathbf{D}^* \rangle}{\langle \mathbf{v}^*_{\boldsymbol{eff}} \rangle} = \frac{\langle \boldsymbol{\kappa}^* \rangle}{\langle \boldsymbol{\nabla}^*\boldsymbol{\kappa}^* \rangle} = \frac{\langle \boldsymbol{\kappa}^* \rangle}{\frac{\langle \partial \boldsymbol{\kappa}^* \rangle}{\partial l^*}}$. Upon a hypothesis of slow-varying conductivity changes along the characteristic lattice content for the target superlattice l^*, this relation could reveal a conserved quantity about the characteristic length for a given system as plotted in Fig. 3**g**, i.e., $\frac{r^*}{\langle \mathrm{Pe} \rangle} \to l^*$ and $\frac{\langle \partial \boldsymbol{\kappa}^* \rangle}{\partial r^*} \to \frac{\langle \boldsymbol{\kappa}^* \rangle}{l^*}$. Then, the non-dimensional expression can be further rewritten as

$$\left(\kappa^*_{rr}\frac{\partial^2\psi^*}{\partial r^{*2}} + \kappa^*_{r\theta}\frac{\partial^2\psi^*}{\partial r^*\partial\theta^*} + \frac{\kappa^*_{\theta\theta}}{r^*}\frac{\partial^2\psi^*}{\partial\theta^{*2}} + \frac{\kappa^*_{\theta r}}{r^*}\frac{\partial^2\psi^*}{\partial r^*\partial\theta^*}\right) + \langle \mathrm{Pe} \rangle\frac{\langle \mathbf{D}^* \rangle}{r^*}\cdot\left(\boldsymbol{\nabla}^*\psi^*\right) - \frac{\partial\psi^*}{\partial\langle \mathrm{Fo} \rangle} = a^*. \tag{S21}$$

5. Critical incident wavenumber for field localization

The localization of thermal field under an incident temperature wave is the critical property induced by moiré flat bands at non-Pythagorean angles. However, such behaviors would be suppressed once the incident wave energy is not

large enough to motivate the localized modes. That is, the incident energy should match the lowest energy of the in-plane moiré superlattice for supporting the flat bands. That is, a threshold value exists to realize the mode matching, when the incident energy and the in-plane moiré superlattice energy are balanced, i.e., $E_{inc,z} = E_{moire}$. Here, the incident energy can be described as $E_{inc,z} = \nabla\left(\kappa_z \nabla T(z,t)\right) - \rho c \frac{\partial T(z,t)}{\partial t}$, where κ_z, ρ, and c respectively denote the thermal conductivity, density, and specific heat of the medium for providing the source along z-direction. Taking the temperature wave $T(z,t) = 353 + 80\mathrm{e}^{i\left(\frac{2\pi z}{\lambda_{z,inc}} + \frac{2\pi}{t_{z,inc}} t\right)}$ into the incident energy, we have $E_{inc,z} = iD_z k_{z,inc}^2$, $D_z = \frac{\kappa_z}{\rho c}$, and $k_{z,inc} = \frac{2\pi}{\lambda_{z,inc}}$. Here, $\lambda_{z,inc}$ and $t_{z,inc}$ are the effective wavelength and modulated period of the incident temperature wave. Besides, an effective wave velocity for the temperature field propagation can be determined with $v_{z,tem} = \frac{\lambda_z}{t_z}$ according to the geometrical property of h_p, thus lead to the frequency of $f_{inc} = \frac{v_{z,tem}}{\lambda_{z,inc}}$. For the in-plane energy at the interface, $E_{moire} = a + a_r$. Under balanced energy, we can achieve the following relation

$$|iD_z k_z^2| = \left|\left(i(\mathbf{k}\cdot\mathbf{k})D(\mathbf{r}) + \mathbf{k}\cdot\nabla D(\mathbf{r})\right) + \left(i\left(\mathbf{k}'\cdot\mathbf{k}'\right)D\left(\mathbf{r}'\right) + \mathbf{k}'\cdot\nabla D\left(\mathbf{r}'\right)\right)\right|. \tag{S22}$$

Then, the following relation can be obtained

$$D_z k_z^2 = \sqrt{\left((\mathbf{k}\cdot\mathbf{k})D(\mathbf{r})\right)^2 + \left(\mathbf{k}\cdot\nabla D(\mathbf{r})\right)^2} + \sqrt{\left(\left(\mathbf{k}'\cdot\mathbf{k}'\right)D(\mathbf{r}')\right)^2 + \left(\mathbf{k}'\cdot\nabla D(\mathbf{r}')\right)^2}. \tag{S23}$$

Due to the inhomogeneous conductivity at the interface and the rotational symmetry of a single site in each quadrant, we have the first-order term $\mathbf{k}\cdot\nabla D(\mathbf{r}) = 0$ when all the points in the four quadrants (Fig. S1) are involved in a unit cell. For simplification, we take the average diffusivity $\langle D(\mathbf{r})\rangle \to \frac{\kappa_0}{\rho c}$, and then Eq. (S23) becomes

$$k_z^2 = \frac{\sqrt{\left((\mathbf{k}\cdot\mathbf{k})\langle D(\mathbf{r})\rangle\right)^2} + \sqrt{\left(\left(\mathbf{k}'\cdot\mathbf{k}'\right)\langle D(\mathbf{r}')\rangle\right)^2}}{D_z} = 2\left(k_x^2 + k_y^2\right)\frac{\langle D(\mathbf{r})\rangle}{D_z}. \tag{S24}$$

As defined in the main content, the wavenumbers of the superlattice are $k_x = \frac{2\pi}{l_s}$ and $k_y = \frac{2\pi}{l_s}$, the threshold $k_{z,0} = \sqrt{2\frac{\langle D(\mathbf{r})\rangle}{D_z}}\frac{2\pi}{l_s}$. In actual experiments, we adopt the same material as the fins to support the source for providing temperature waves, that is the diffusivity $D_z = \frac{\kappa_0}{\rho c}$. In this case, a scale parameter for characterizing the imposed energy and the eigenenergy of the thin layer in actual experiments $n = \frac{k_{z,inc}}{k_z}$. The threshold value of n occurs when the $k_{z,imposed} = k_{z,0}$ and results in $f_{threshold} = n_{threshold} f$. Note that, $n_{threshold} = \frac{k_{z,0}}{k_z} = \frac{\sqrt{2}\lambda_{z,inc}}{l_s}$ depends on the lattice

constants at corresponding twisted angles (Fig. 4**h** and **i** of the main content). Localized behaviors can be motivated if and only if the $\lambda_z < \lambda_{z,0}$ when $f_{inc} > f_{threshold}$.

6. Effective dispersion of the temperature propagation modes

In Figs. 4**a** ~ **c** of the main text, we present experimental measurements of temperature fields under a pulsed point source operating at 150 Hz. The corresponding band structures are plotted in Fig. S3 and the numerical simulations under the same energy input are shown in Fig. S4, which exhibits well agreement with the experimental results. Notably, the two commensurate superlattices exhibit anisotropic thermal dissipation rather than omnidirectional spreading, while the incommensurate superlattice demonstrates pronounced thermal localization. To further investigate these propagation behaviors, we perform fast Fourier transform (FFT) analysis to extract the dispersion relations at the driving frequency. The commensurate superlattices exhibit prominent hyperbolic dispersion patterns, indicating dominant energy propagation along nearly biorthogonal directions (Figs. S4**d** and **e**). As a result, the real-space temperature profiles are confined within anisotropic and non-circular regions, which consistent with the presence of non-flat bands. In stark contrast, the dispersion spectrum of the incommensurate superlattice shows significantly reduced (near-zero) values, indicating vanishing group velocity. This near-zero group velocity is a hallmark of flat-band behavior corresponding to the observed temperature localization under minimal dispersion.

7. Experimental setups

To implement the desired conductivity configuration at each site within a unit cell, we begin with a thin square epoxy plate of thickness of h_p = 1 mm and a side length of $l_p = \frac{l}{2} = 5$ mm. The top surface of this plate serves as the coupling platform for heat exchange at the interface of the bilayer structure. On the bottom side, we configure alternating epoxy fins of varying heights (h_f) to create the effective conductivity distribution (Figs. 3**b** and **c** of the main content). Upon energy conservation between each site and its corresponding fin under identical heat sources, we have $Q_i = \int \kappa_i \nabla^2 T dV_i = \int \kappa_p \nabla^2 T dV_{fin,i} = Q_{fin,i}$ and $i = A$ or B representing the target site. Then, the conductivity along the radial direction in

each site can be effectively determined by $\kappa_{i,r} = \kappa_p \frac{Q_{fin,i}}{Q_i}$. Given the uniform heat exchange area between each site and its associated fin, the fin height directly dominates the local conductivity, leading to the simplified relation of $\kappa_{i,r} \to \kappa_p \frac{h_{f,i}}{h_p}$. In this case, the heat exchange area between the plate and the fin (from the base to height h_f), follows a proportional relation to the area of the thin plate, i.e., $\frac{S_{A,h}}{S_p} = \frac{l_{A,h}^2}{l_p^2}$, where $S_{A,h}$ and $l_{p,h}$ respectively denote the heat exchange area and side length of the fin at tailored height of site A. To represent this configuration, we employ a tapered fin structure for site A to realize a smooth conductive gradient across the plate (Fig. 3**c**). In contrast for site B with near-zero conductivity, anisotropic effects are negligible. Therefore, we leave the corresponding area of the thin plate in direct contact with air, maintaining a thermal conductivity of $\kappa_B = 0.0025$ W·m^{-1}·K^{-1} without additional structures vertical structure ($h_{f,B} = 0$). In this case, we have $\kappa_A = 10$ W·m^{-1}·K^{-1} and $\kappa_B \to 0$ at each site center, while the conductivity of the symmetry center $\kappa_0 = \frac{|\kappa_A + \kappa_B|}{2}$ is 5 W·m^{-1}·K^{-1} for each experimental unit cell. By periodically arranging and vertically stacking these two conductive layers with specific twist angles, we construct a platform to experimentally demonstrate the emergence of moiré patterns at the bilayer interface. The linear superposition of their conductivity distributions produces an inhomogeneous moiré potential, with the highest and lowest temperature amplitudes confined to regions where the conductivity gradient approaches zero.

In the demonstrations of moiré patterns presented in Fig. 3, a constant heat flux is applied perpendicular to the interface of the entire sample. Specifically, a heat source at 373 K is applied to the bottom surface, while a cooling source at 273 K is imposed on the top surface of the bilayer system. The resulting temperature profiles shown in Fig. 3 are recorded at the interface after 30 minutes of heating and cooling. To investigate the localized modes illustrated in Figs. 4**a** ~ **c** of the main content, we employ a thermal pulsing point source that generates a temperature wave described by $T(z,t) = 353 + 80e^{i\left(\frac{2\pi z}{\lambda_{z,inc}} + \frac{2\pi}{t_{z,inc}}t\right)}$, where the excitation frequency is given by $f_{inc} = \frac{v_{z,tem}}{\lambda_{z,inc}} = 150$ Hz. Such a point source replaces the global heating strategy in Fig. 3. The heating duration is again set to 30 minutes. Localized and delocalized thermal modes can be clearly identified based on the spatial extent of a designated isothermal contour line at the interface.

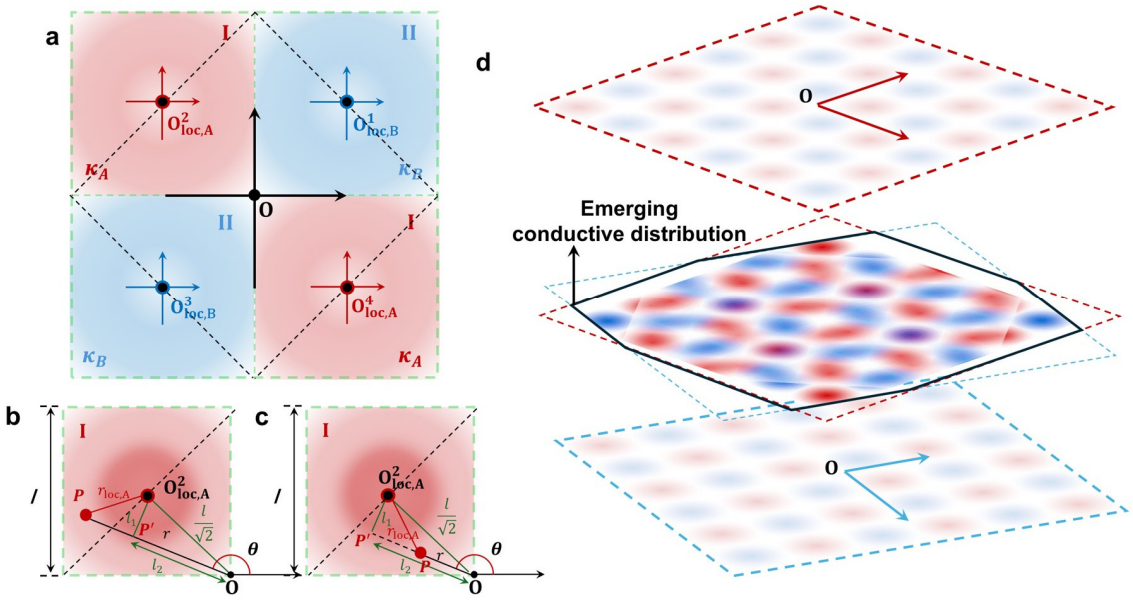

Fig. S1. Schematic of the conductivity distributions. a. Conductivity distribution of a four-site unit cell in a monolayer. **b** and **c** present the two types of the local conductivity of a selected point in one site. **d** indicates the schematic of generating the moiré conductivity distributions via stacking two monolayers with a tailored twist angle.

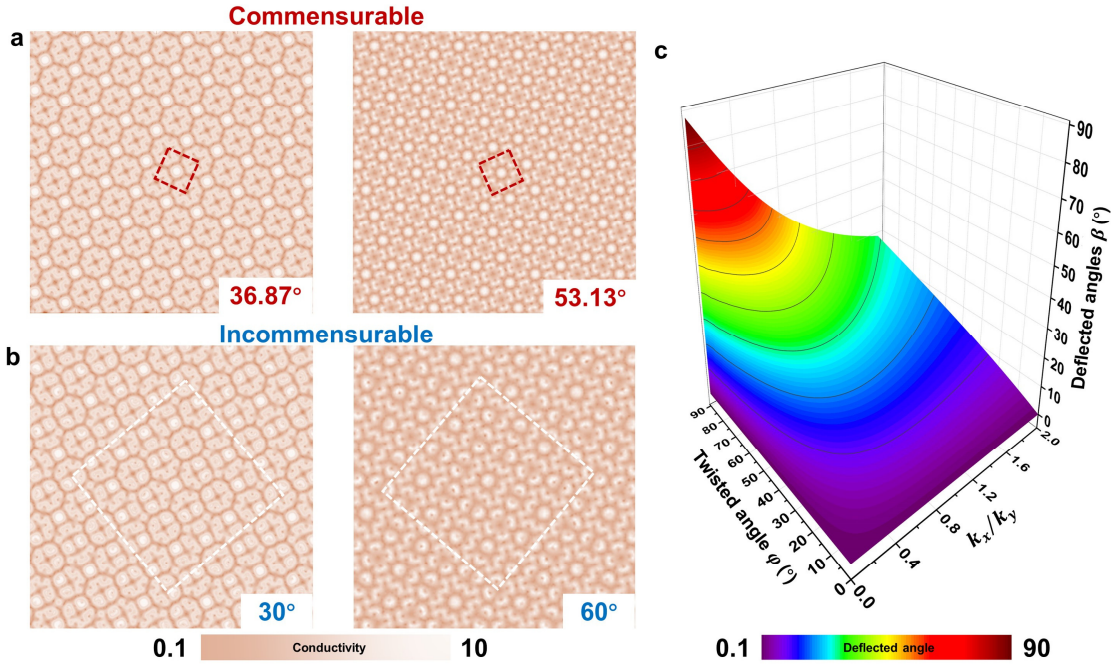

Fig. S2. Moiré patterns of the cases at different twisted angles centered around $\frac{\pi}{4}$. a. The moiré patterns of commensurable lattices at the twisted angles of 36.87° and 53.13°. The red-dashed boxes indicate the unit cell of the superlattice. **b.** The moiré patterns of incommensurable lattices at the twisted angles of 30° and 60°. The white-dashed boxes indicate the effective unit cell of the quasi-crystals. **c** plots deflected angle of the moiré patterns under the changing twisted angles and wavevectors.

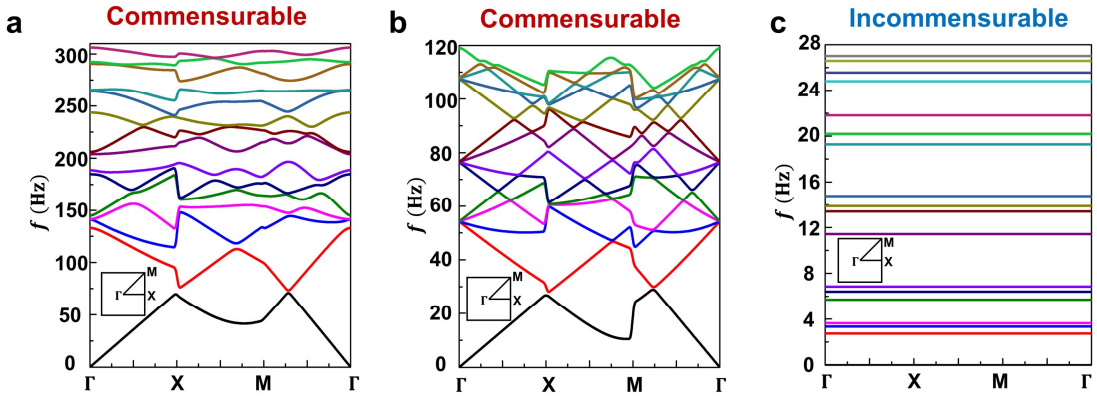

Fig. S3. Effective band structures of the conductive moiré superlattice. a ~ c respectively present the effective band structures of the first Brillouin zones at different angles.

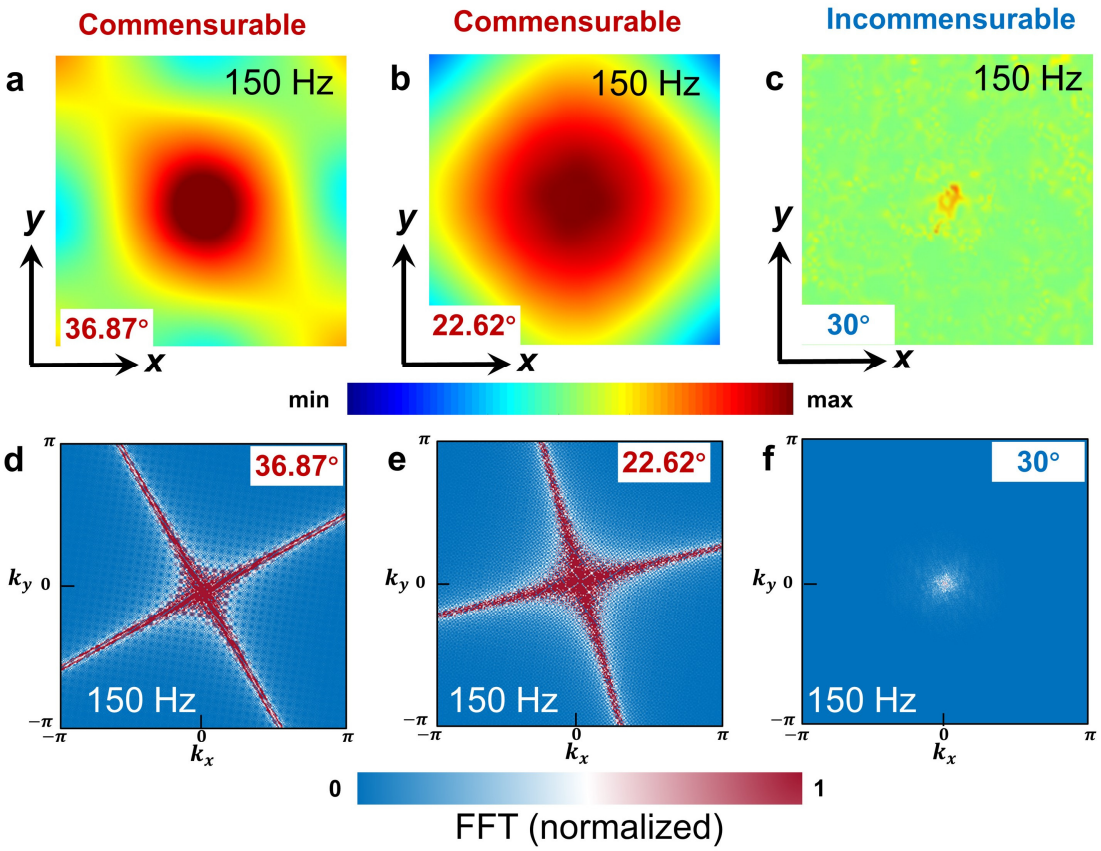

Fig. S4. Effective dispersion of the temperature propagation modes. a ~ c present the numerical temperature fields corresponding to those in Figs. 4**a** ~ **c** of the main contents under a pulsing point source with the incident frequency of 150 Hz. **d** ~ **f** denote the effective dispersions after FFT of the three cases.